JOURNAL OF APPLIED CRYSTALLOGRAPHY

Volume 54 (2021)

Supporting information for article:

A high-flux automated laboratory SAXS instrument optimized for solution scattering

Jeppe Lyngsø and Jan Skov Pedersen

S1. 2D spectra from the HyperSAXS

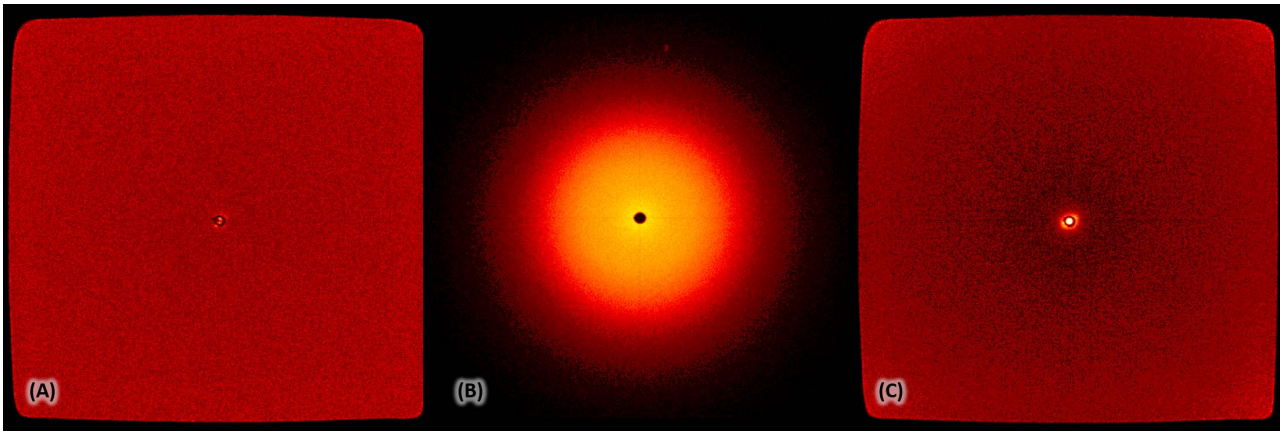

Figure S1: 2D SAXS data as represented by the Bruker SAXS NT software. (A) Milli-Q water subtracted the transmission-scaled empty capillary scattering (600 s). (B) Raw glassy carbon data (600 s). (C) Polystyrene standard raw data (100 s).

S2. Recent upgrades of the rotating-anode-based SuperSAXS instrument (Pedersen, 2004)

The old SAXS instrument at Aarhus University, which is the original proto-type of the NanoSTAR U instrument of Bruker AXS, has been upgraded several times since it was described in the publication in 2004 (Pedersen, 2004). The filament of the rotating Cu anode source was changed to a 0.1×1.0 mm^2 filament and the power was at the same time reduced to 0.99 kW (22 mA and 45 kV) in 2003-2004. At about the same time, a semitransparent beamstop with a similar design as described for the HyperSAXS instrument was installed. For the cupper-based (Cu $K_\alpha = 8.05$ keV) source, the optimal attenuator material is nickel (Ni), which has the absorption K-edge at 8.33 keV. A scatterless octagonal slit was introduced in 2010 and a flow-through cell was installed in 2013. The instrument has relatively short standard Göbel mirrors and the first pinhole is therefore a ⌀ 1.0 mm pinhole, whereas the second scatterless slits has dimensions similar to the one in the new instrument (1.52 mm diagonally and ~1.40 mm between opposite jaws). The distance between the pinhole and slits is 1410 mm, the sample-to-detector distance is 640 mm, and the beamstop size is ⌀ 3.0 mm. For this configuration and power of the source, the flux at the sample position is $1\text{-}2 \times 10^8$ ph s^{-1}, i.e. about 10 times higher than for the originally reported 3-pinhole collimation. The latest upgrade is the installation of a VÅNTEC-500 detector (Bruker AXS) in January 2017.

S3. Materials and methods for additional samples

S3.1. Bovine serum albumin

Heat-shock fractionated bovine serum albumin (BSA) ≥ 96% (A3912, Sigma-Aldrich) was solubilized in phosphate-buffered saline (PBS) buffer, 20 mM phosphate, 50 mM NaCl, pH 7.4 at a concentration of 0.84 mg mL^{-1}. The freshly prepared sample was measured at 20 °C.

S3.2. Low-density lipoprotein particles

A far more complex protein-containing sample is also included, data from (Maric *et al.*, 2017). Purified low-density lipoprotein (LDL) particles pooled from three healthy patients were solubilized in 25 mM Tris, 150 mM NaCl, 0.5 mM EDTA, pH 7.4 buffer. The LDL solution was measured in a temperature scan at: 5, 10, 15, 20, 25, 30, 35, 37, and 40 °C and exposed for 1200 s at each temperature step. The total protein concentration (in the outer shell of the particles) was estimated from Bradford assay to: $c_{prot} = 0.4$ mg mL^{-1}. The LDL particles, however, additionally consist of various phospholipids (mainly phosphatidylcholine (PC) and sphingomyelin (SM)), cholesteryl esters, and triglycerides.

S3.3. PEG polymer solution

Poly(ethylene glycol) (PEG), $\bar{M}_n = 4{,}600$ g mol^{-1} (373001, Sigma-Aldrich) was dissolved in Milli-Q water at a concentration of 1.0 wt% at room temperature and left for equilibration. The polymer sample was measured at 20 °C for 1800 s with Milli-Q water as background.

S4. Results

Bovine serum albumin was fitted with the in-house program WLSQ_PDBx, now with an added cluster structure factor where a dimer fraction was included in the PDB model fitting to account for the known possible disulfide-bonded dimers forming in BSA solutions (Jordan *et al.*, 1994; Svergun & Koch, 2003; Rombouts *et al.*, 2015; Morishima *et al.*, 2020); see Fig. S2). The BSA data showed clear deviations from pure monomer scattering, however, including a dimer contribution allowed for proper fitting the logarithmically binned data with the crystal structure, 4F5S (Bujacz, 2012), of BSA with a $\chi^2 = 0.78$. The monomer/dimer fraction was estimated to 73.6% monomers and 26.4% dimers with a center-to-center distance for the monomers within the dimers of 61.6 Å. CRYSOL was intentionally used "inappropriately" to perform a monomer structure fit to show the discrepancy from the monomeric state for this sample, $\chi^2 = 2.93$ (no constant added). This sample

would need a size-exclusion chromatography (SEC) purification step for separation into monomers and dimers before using it as a true monomer protein standard.

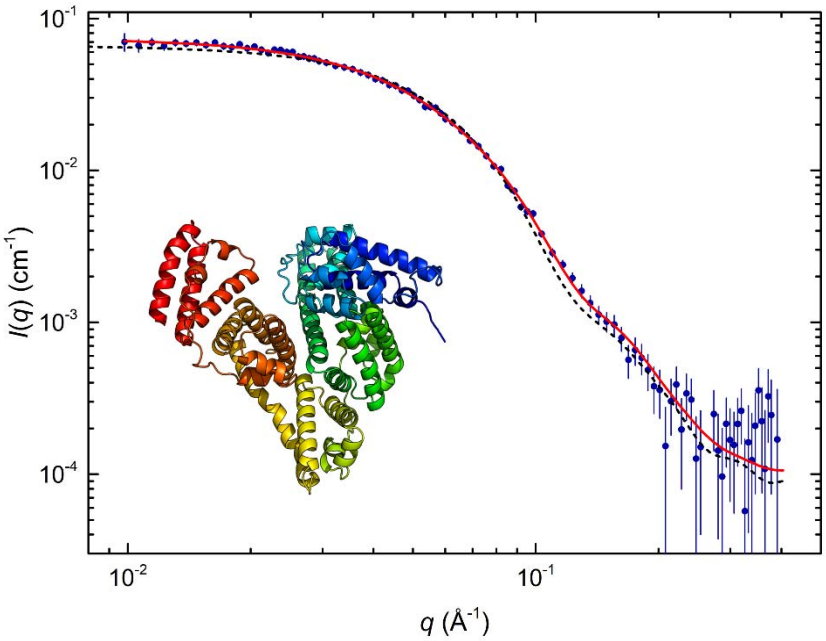

Figure S2: Experimental SAXS data for a standard low-concentration (0.84 mg mL^{-1}, pH 7.4) bovine serum albumin (BSA) protein solution at 20 °C with 600 s exposure time (blue dots with error bars), data logarithmically binned. Fits to crystallographic monomer model (inset) calculated using *CRYSOL*, no constant added (black dashed) and in-house *WLSQ_PDBx*, constant added with a dimer-cluster structure factor contribution (red line).

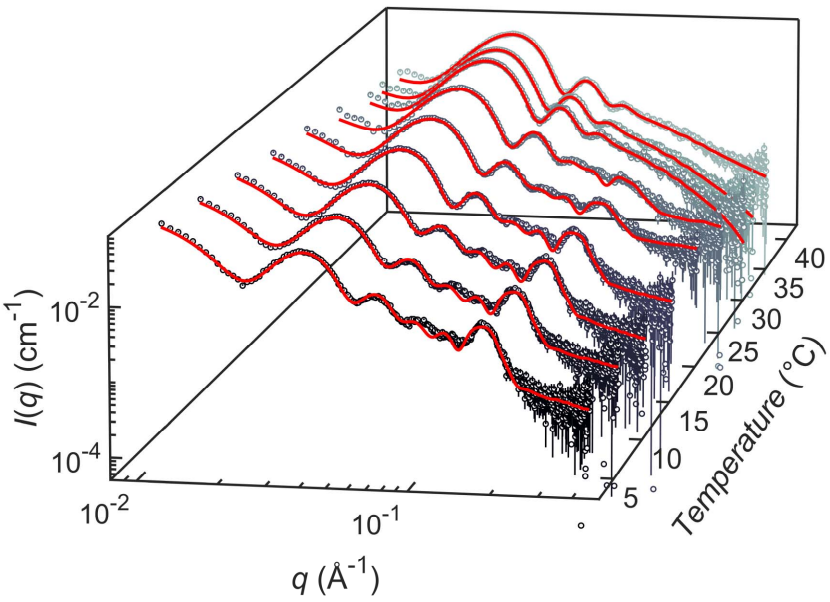

Figure S3: Experimental SAXS data for low-density lipoprotein solutions at pH 7.4 with an estimated total protein concentration: c_{prot} = 0.4 mg mL^{-1}, 5-40 °C, and 1200 s exposure time (open circles with error bars). Core-shell superellipsoid of revolution with internal layering model fits to data (red lines). Data and fits according to (Maric *et al.*, 2017).

The non-re-binned feature-rich SAXS spectra of the LDL particles were fitted with the model of a core-shell super-ellipsoid with a lipid core and internal cholesteryl ester layering from (Maric *et al.*, 2017), Fig. S3. A temperature scan on the same sample was performed in order to follow the reversible melting of the internal layered structure and the following overall shape transition of the particles. Shape parameter, particle dimensions, and relative electron densities were extracted as a function of temperature from the model fits. This model, based largely on new Cryo-TEM imagery inputs, allows a complete description of LDL SAXS data and the changes in particle structure with temperature.

A standard PEG solution of 1 wt% was measured showing the expected polymer scattering behavior and an additional up-turn at low q from a co-existing fraction of larger loosely aggregated polymers in the sample, Fig. S4. The aggregation is a known phenomenon in aqueous solutions of alcohol-terminated poly(ethylene oxide) (Ho et al., 2003; Hammouda et al., 2004). The polymer scattering was fitted with the classical Debye form factor (Debye, 1947) for Gaussian polymer chains yielding the q^{-2}-dependency at intermediate q; a small constant background was added. From the fit a radius of gyration of $R_g = 24.5 \pm 0.4$ Å was determined in good agreement with the theoretical value of $R_g = \sqrt{C_\infty M m_0^{-1} l_0^2/6} = 24.4$ Å for linear PEO polymers, with a molecular weight of 4,600 g mol^{-1}, a Kuhn length of $C_\infty l_0 = 5.1$ Å $\times$ 1.49 Å $= 7.6$ Å (Aharoni, 1983), and a calculated average molecular weight per bond, m_0, of 14.68 g mol^{-1}.

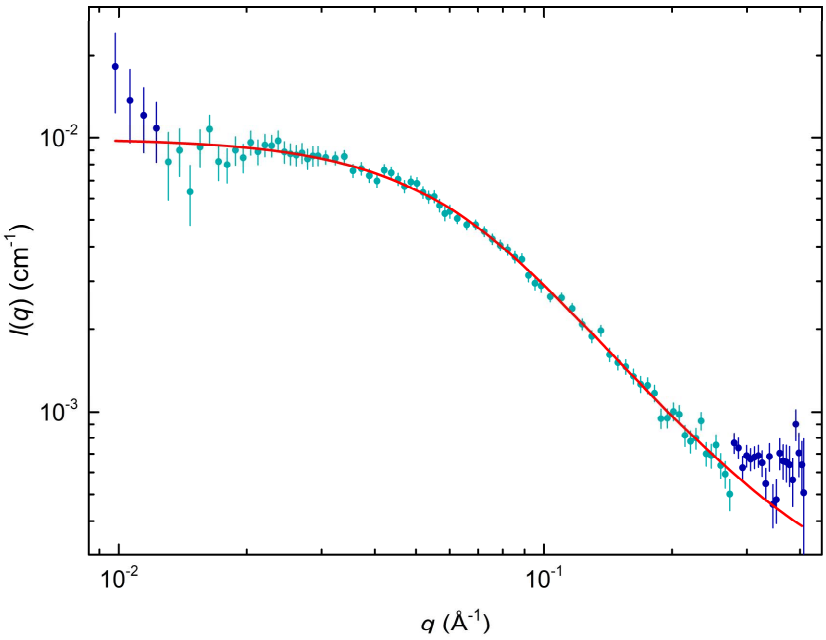

Figure S4: Experimental solution SAXS data for 1.0 wt% poly(ethylene oxide), $\bar{M}_n = 4{,}600$ g mol^{-1}, in water at 20 °C, and 1800 s exposure time (navy and teal dots with error bars), data logarithmically binned. Fit with Gaussian chain polymer model (q^{-2}) in the region indicated by teal (red line).

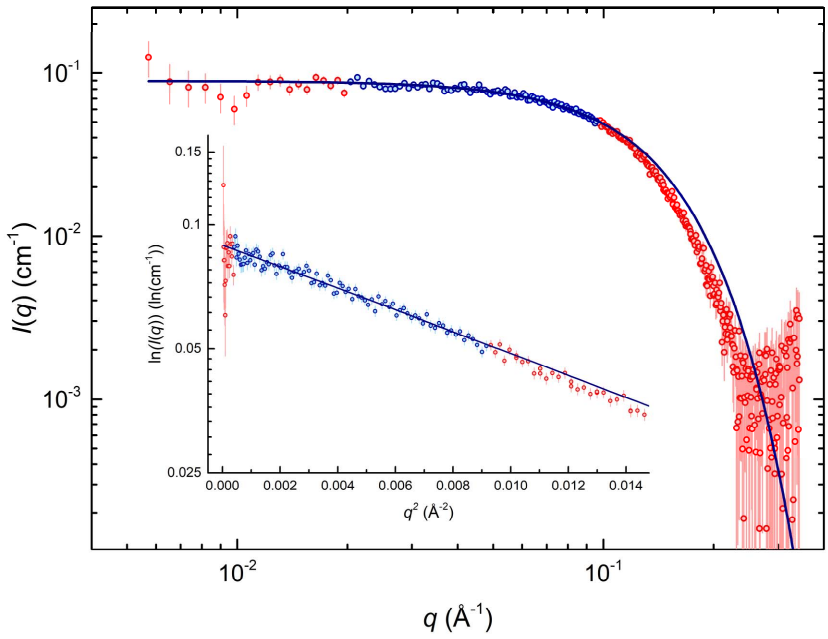

Figure S5: Guinier fit (navy lines) to low-q configuration lysozyme data, 10.7 mg mL^{-1}, pH 5.0, 1800 s exposure time (red circles). Fitted q range indicated by blue circles, qR_g limits: $0.28 - 1.30$. $\chi^2 = 1.0$ with a $R_g = 13.5 \pm 0.1$ Å. Inset: Guinier plot showing the fitted linear range.

References:

Aharoni, S. M. (1983). *Macromolecules*. **16**, 1722–1728.
Bujacz, A. (2012). *Acta Crystallogr. Sect. D Biol. Crystallogr.* **68**, 1278–1289.
Debye, P. (1947). *J. Phys. Colloid Chem.* **51**, 18–32.
Hammouda, B., Ho, D. L. & Kline, S. (2004). *Macromolecules*. **37**, 6932–6937.
Ho, D. L., Hammouda, B. & Kline, S. R. (2003). *J. Polym. Sci. Part B Polym. Phys.* **41**, 135–138.
Jordan, G. M., Yoshioka, S. & Terao, T. (1994). *J. Pharm. Pharmacol.*
Maric, S., Lind, T. K., Lyngsø, J., Cárdenas, M. & Pedersen, J. S. (2017). *ACS Nano*. **11**, 1080–1090.
Morishima, K., Okuda, A., Inoue, R., Sato, N., Miyamoto, Y., Urade, R., Yagi-Utsumi, M., Kato, K., Hirano, R., Kujirai, T., Kurumizaka, H. & Sugiyama, M. (2020). *Commun. Biol.* **3**, 294.
Pedersen, J. S. (2004). *J. Appl. Crystallogr.* **37**, 369–380.
Rombouts, I., Lagrain, B., Scherf, K. A., Lambrecht, M. A., Koehler, P. & Delcour, J. A. (2015). *Sci. Rep.* **5**, 12210.
Svergun, D. I. & Koch, M. H. J. (2003). *Reports Prog. Phys.* **66**, 1735–1782.